THE JOURNAL OF PHYSICAL CHEMISTRY C

pubs.acs.org/JPCC Article

Structure–Property Study of Homoleptic Zinc(II) Complexes of Di(arylethynyl) Azadipyrromethene as Nonfullerene Acceptors for Organic Photovoltaics: Effect of the Aryl Group

Chunlai Wang, Muyuan Zhao, Arnold L. Rheingold, and Geneviève Sauvé*

Cite This: J. Phys. Chem. C 2020, 124, 8541–8549 Read Online

ACCESS | Metrics & More | Article Recommendations | Supporting Information

ABSTRACT: Azadipyrromethene-based zinc(II) complexes were demonstrated to be promising molecular organic semiconductors for electronic applications due to their easy preparation, tunable structures, and high electron affinity. The first successful such complex incorporated phenylethynyl groups at the pyrrolic positions, which red-shifted the absorption spectra of zinc(II) bis(tetraphenyl azadipyrromethene) and improved the morphology in blends with poly(3-hexylthiophene) (P3HT). We recently discovered that replacing the phenyl group in the pyrrolic positions with the larger 1-naphthyl group [Zn(L2)$_2$] increases the crystallinity and improves the organic photovoltaic (OPV) performance. In this work, two more aryl groups were explored to further investigate the relationship between the aryl groups in the pyrrolic position and electronic properties: naphthyl with a different anchoring site, 2-naphthyl [Zn(L3)$_2$], and a larger aryl group, 9-phenanthrenyl [Zn(L4)$_2$]. The larger aryl group slightly improved the absorptivity, red-shifted the absorption spectra, and led to different packing modes in crystals with most intermolecular $\pi-\pi$ stacking interactions being of T-shaped-type involving the pyrrolic aryl group of one complex. Of the series, 1-naphthyl gave the highest crystallinity. The organic photovoltaic (OPV) power conversion efficiency (PCE) of Zn(L3)$_2$ and Zn(L4)$_2$ when blended with P3HT was 3.7 and 3.4%, respectively, both lower than that of Zn(L2)$_2$ (PCE of 5.5%) due to the higher trap-assisted recombination and less favorable morphology. The charge carrier mobility in these complexes was also relatively low, also limiting the performance. Single-point energy calculations point to low overlap integrals as a cause for the low mobility. The aryl group anchoring position and size, therefore, have a large effect on the properties in these systems, but do not appear to significantly enhance intermolecular interactions.

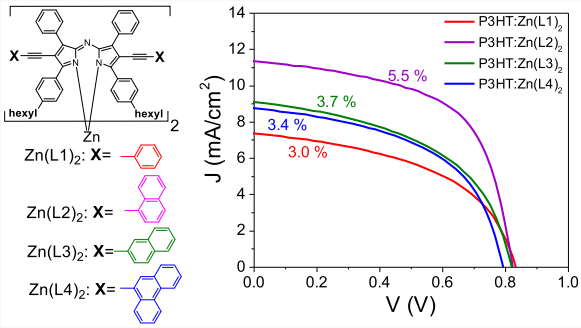

Downloaded via CASE WESTERN RESERVE UNIV on June 23, 2020 at 18:48:02 (UTC).
See https://pubs.acs.org/sharingguidelines for options on how to legitimately share published articles.

■ INTRODUCTION

Azadipyrromethenes (ADPs, Figure 1) are a class of monoanionic bidentate ligands with strong absorption in the visible and near-infrared (IR) range and low reduction potentials.[1,2] Their synthesis is simple and uses inexpensive starting materials.[1] Their optical properties have been tuned through structural modifications and chelation.[1,3,4] The most-studied systems are BF_2^+ chelates, with applications in photodynamic therapy, bioimaging, and light harvesting. Several BF_2^+ chelates were shown to be promising donor materials when paired with fullerene (C_{60}) as an electron acceptor in organic photovoltaics (OPVs).[5−8] We have previously demonstrated that homoleptic zinc(II) complexes of azadipyrromethenes are promising candidates as non-fullerene acceptors for solution-processed organic OPV applications.[9,10] The presence of pyrrolic substituents, such as phenylethynyls in Zn(WS3)$_2$ (Figure 1), red-shifts the absorption spectra and increases electron affinity.[11] This complex has a high absorption between 600 and 800 nm, complementary to the cheapest and most-studied conjugated polymer electron donor, regioregular poly(3-hexylthiophene) (P3HT).[12] When blended with P3HT, Zn(WS3)$_2$ behaves as an electron acceptor. The complex nonplanar distorted tetrahedral molecular shape helps tune self-aggregation and enables favorable nanophase separation from P3HT, resulting in a good performance in OPVs.[9,13] However, the performance is currently not high enough for practical applications.

To improve the performance, it is necessary to understand the structure–property relationships in these complexes. We have established that the presence of arylethynyl groups at the pyrrolic positions is essential to increase the conjugation of the complex and obtain favorable phase separation from P3HT.[11] Replacing the triple bond with a double bond, on the other hand, increases the energy levels and lowers the performance.[14] Fluorination at the para position of the phenylethynyl

Received: January 15, 2020
Revised: March 21, 2020
Published: March 25, 2020

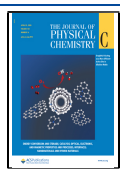

ACS Publications © 2020 American Chemical Society

https://dx.doi.org/10.1021/acs.jpcc.0c00401
J. Phys. Chem. C 2020, 124, 8541−8549

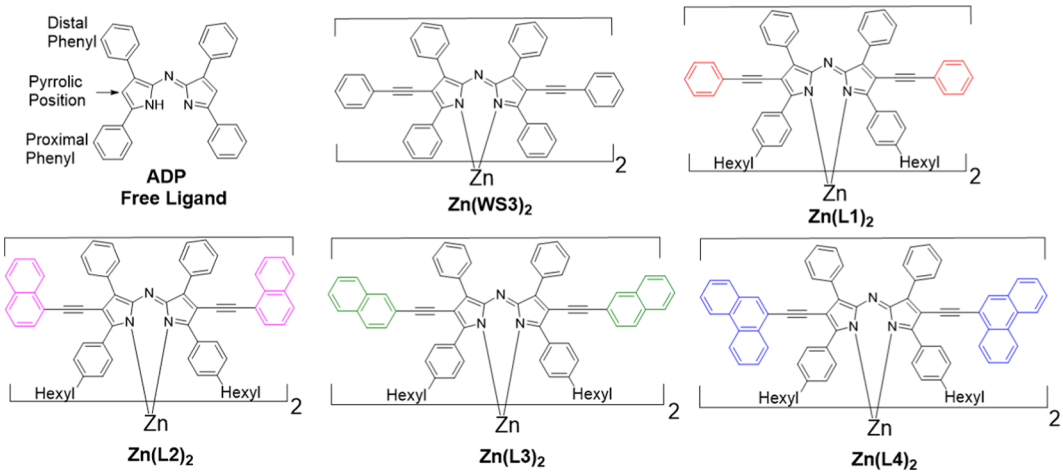

Figure 1. Chemical structure of the ADP-free ligand and ADP-based zinc(II) complexes.

Scheme 1. Synthesis Scheme for Zinc(II) Complexes: Zn(L1−L4)$_2$[a]

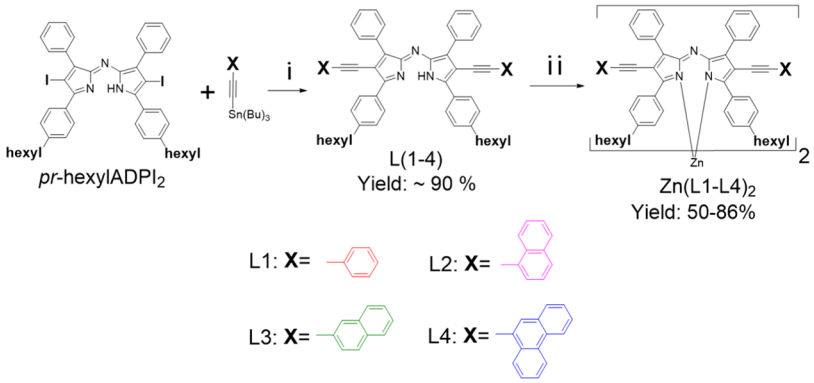

[a](i) Pd(PPh$_3$)$_4$, xylenes, 125 °C, 8 h, (ii) tetrahydrofuran (THF), NaH, 55 °C, 4 h, followed by CH$_2$Cl$_2$, ZnCl$_2$/MeOH, 25 °C, 24 h.

improves the performance and electron mobility.[15] These complexes tend to be amorphous, making it hard to obtain a crystal structure. The first crystal structure of a Zn(WS3)$_2$ derivative published was that of the complex with fluorine at the para distal phenyls, which showed intermolecular interactions between the pyrrolic phenyls of two neighboring molecules.[16] This suggested that the aromatic group on the pyrrolic substituent plays an important role in intermolecular $\pi-\pi$ interactions and charge transport. To test this hypothesis, the phenyl in the pyrrolic phenylethynyl groups was replaced with the larger 1-naphthyl group.[10] Since introducing the larger aryl group reduced the solubility significantly, hexyl solubilizing groups were also added at the para position on the proximal phenyls. Interestingly, both the hexyl groups and the larger aryl group increased the crystallinity and OPV performance, with the largest power conversion efficiency (PCE) of 5.5% obtained with P3HT:Zn(L2)$_2$ blends. Moreover, the Zn(L2)$_2$ complex did not require any column purification. Combined with its simple synthesis, it resulted in a very low synthetic complexity, which leads to a relatively high industrial accessibility.[10] Here, we explored two more aryl groups: 2-naphthyl [Zn(L3)$_2$] and 9-phenanthrenyl [Zn(L4)$_2$]. The optical, electrochemical, and thermal properties were explored and compared with those of Zn(L1)$_2$ and Zn(L2)$_2$. All of the new complexes formed crystals, enabling the study of their crystal structure in the solid state. Photovoltaic and charge-transport properties were also investigated to further establish the structure-property relationships for this series.

■ RESULTS AND DISCUSSION

Synthesis. Scheme 1 summarizes the synthesis of Zn(L1)$_2$, Zn(L2)$_2$, Zn(L3)$_2$, and Zn(L4)$_2$ [abbreviated as Zn(L1−L4)$_2$]. The synthesis of Zn(L1)$_2$ and Zn(L2)$_2$ was previously published by us.[10] Zn(L3)$_2$ and Zn(L4)$_2$ were synthesized starting with the precursor pr-hexylADPI$_2$,[10] followed by reacting with appropriate tributyl tin compounds using Stille coupling conditions to give different pyrrolic substituents.[11] The Sonogashira coupling reaction has been used as an alternative for obtaining pyrrolic substituents. However, chelation between Cu$^+$ and ADP occurs under basic conditions and leads to catalyst (CuI) poisoning and generation of ADP-based Cu$^+$ complex byproducts, resulting in low yields of the desired product. The ligands L3 and L4 were purified by washing with methanol and were isolated as dark blue powders in very good yields (~90%). Similar to L1 and L2, L3 is slightly soluble in nonpolar solvents, such as hexanes, and readily soluble in polar solvents, such as acetone and dichloromethane. L4 is insoluble in most organic solvents, most likely due to the aggregation induced by the large aromatic groups in the pyrrolic positions. The identity and purity of new ligands were confirmed by ^{1}H NMR, matrix-assisted laser desorption ionization time-of-flight mass spectrometry (MALDI-TOF MS) (see the Supporting Information) except for L4, whose

https://dx.doi.org/10.1021/acs.jpcc.0c00401
J. Phys. Chem. C 2020, 124, 8541−8549

identity and purity were only confirmed by MALDI-TOF MS (see the Supporting Information) due to the low solubility in organic solvents.

The zinc(II) complexes were synthesized using our published procedure in good yields.[16] To save resources, we explored purifying the complexes by solvent washing instead of column chromatography. Only $Zn(L2)_2$ could be purified satisfactorily by washing with solvents. In contrast, the other zinc complexes required column chromatography to separate the products from their unreacted ligands. $Zn(L3)_2$ and $Zn(L4)_2$ were collected from the first blue-colored fractions. The yields of $Zn(L3)_2$ (61%) and $Zn(L4)_2$ (55%) were lower than the yield of $Zn(L2)_2$, due to losses during purification. The identity and purity of all complexes were confirmed by ^{1}H NMR, MALDI-TOF MS, and elemental analysis (see the Supporting Information).

Optical and Electrochemical Properties. The UV−vis absorption spectra of $Zn(L1-L4)_2$ in chloroform are shown in Figure 2 and summarized in Table 1. The spectra of all zinc complexes are similar, with a small red-shift and increase in absorptivity observed as the size of the aryl group increased. The λ_{max} of $Zn(L1)_2$ is 679 nm and it red-shifts to 700 nm for $Zn(L2)_2$, 692 nm for $Zn(L3)_2$, and 705 nm for $Zn(L4)_2$. The absorptivity of the visible band also increases from 1.35×10^5 M^{-1} cm^{-1} for $Zn(L1)_2$ to ~1.40×10^5 M^{-1} cm^{-1} for $Zn(L2)_2$ and $Zn(L3)_2$, and 1.66×10^5 M^{-1} cm^{-1} for $Zn(L4)_2$. The larger red-shift and absorptivity of $Zn(L4)_2$ are consistent with its larger conjugated system. A similar trend in λ_{max} was observed for the film absorption spectra (Figure S10), with λ_{max} increasing from 716 nm for $Zn(L1)_2$ to 727, 721, and 733 nm for $Zn(L2)_2$, $Zn(L3)_2$, and $Zn(L4)_2$, respectively. Table 1 reports the change of λ_{max} observed upon film formation. All complexes red-shift upon film formation, suggesting increased intermolecular interactions in the solid state.

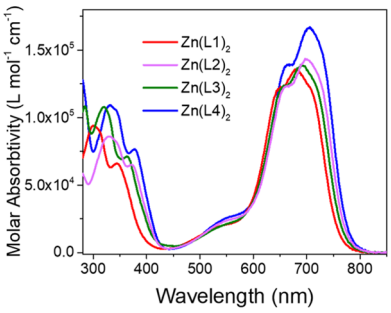

Figure 2. UV−vis absorption spectra of zinc(II) complexes in chloroform.

The cyclic voltammograms (CV) of the zinc(II) complexes in dichloromethane are shown in Figure 3A and summarized in Table 2. The CVs of $Zn(L1-L4)_2$ are similar, with two reversible oxidation and two reversible reduction peaks. Figure 3B summarizes the estimated highest occupied molecular orbital (HOMO) and lowest unoccupied molecular orbital (LUMO) energy levels obtained from the E_{onset} values of the first oxidation and first reduction peaks, respectively. All zinc(II) complexes have both similar LUMO energy levels at around −3.6 eV and similar HOMO at around −5.18 eV. This indicates that the substitution of aromatic groups in the pyrrolic position did not significantly affect the energy levels of these zinc complexes.

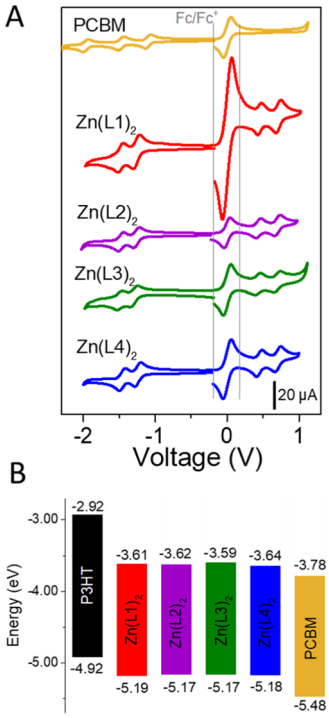

Figure 3. (A) Cyclic voltammograms of PCBM and Zn complexes in the 0.1 M $TBAPF_6$ dichloromethane solution with Fc/Fc^+ as an internal standard ($E_{1/2}$ at 0.0 V). (B) Estimated HOMO and LUMO energy levels were obtained by cyclic voltammetry from the E_{onset} values in dichloromethane, using the value of −4.8 eV for Fc/Fc^+. The energy levels for P3HT were estimated using the oxidation onset in films and the optical gap.

Thermal Properties. The thermal stability of the zinc(II) complexes was investigated by thermal gravimetric analysis (TGA). The thermographs are shown in Figure S11. All zinc(II) complexes were thermally stable, with a 5% weight loss temperature (T5%) in the range of 415−454 °C for $Zn(L1-L4)_2$. The substitution of phenyl with naphthyl or phenanthrenyl groups slightly reduced the T5%. Nevertheless, these T5% values are sufficiently high for most device fabrication conditions.

Figure 4 shows the differential scanning calorimetry (DSC) profiles of the first heating and cooling cycles for single crystals of zinc(II) complexes. The first cooling cycle and subsequent

Table 1. Summary of Optical Properties of Zinc(II) Complexes in the Solution and Film

compound	solution		film		optical gap (eV)	$\Delta\lambda_{max}$ upon film formation
	λ_{max} (nm) (ε, $\times 10^3$ M^{-1} cm^{-1})	λ_{onset} (nm)	λ_{max} (nm)	λ_{onset} (nm)		
$Zn(L1)_2$	300 (94), 344 (66), 650 (122), 679 (135)	760	716	801	1.55	37
$Zn(L2)_2$	330 (86), 373 (65), 664 (123), 700 (143)	775	727	805	1.54	27
$Zn(L3)_2$	320 (110), 363 (71), 659 (124), 692 (139)	771	721	807	1.54	29
$Zn(L4)_2$	332 (110), 378 (76), 665 (139), 705 (166)	779	733	821	1.51	28

https://dx.doi.org/10.1021/acs.jpcc.0c00401
J. Phys. Chem. C 2020, 124, 8541−8549

Table 2. Electrochemical Properties of Zinc(II) Complexes in Dichloromethane[a]

compound	$E_{1/2}$ ox. (V)	E_{onset} 1st ox. (V)	$E_{1/2}$ red. (V)	E_{onset} 1st red. (V)	HOMO/LUMO (eV)	E_{gap} (eV)
$Zn(L1)_2$	0.45, 0.71	0.39	−1.26, −1.49	−1.19	−5.19/−3.61	1.58
$Zn(L2)_2$	0.44, 0.71	0.37	−1.26, −1.48	−1.18	−5.17/−3.62	1.55
$Zn(L3)_2$	0.43, 0.70	0.37	−1.29, −1.50	−1.21	−5.17/−3.59	1.58
$Zn(L4)_2$	0.45, 0.71	0.38	−1.24, −1.46	−1.16	−5.18/−3.64	1.54

[a]Estimated HOMO and LUMO energy levels obtained by cyclic voltammetry from the E_{onset} values in the dichloromethane solution, using the value of −4.8 eV for Fc/Fc^+ versus vacuum.

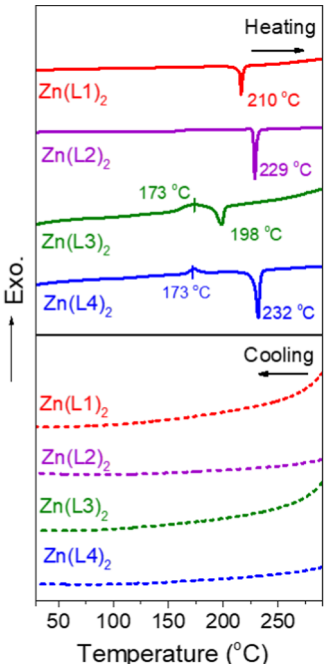

Figure 4. DSC curves for the zinc(II) complexes in the first heating cycle and first cooling cycle.

heating/cooling cycles are featureless. $Zn(L3)_2$ and $Zn(L4)_2$ showed an exothermic peak at 173 °C during the first heating cycle, assigned to the transition from amorphous to crystalline (cold crystallization). No such transition peak was observed in $Zn(L1)_2$ and $Zn(L2)_2$ probably because they were already highly oriented in the solid sample. $Zn(L1–L4)_2$ showed an endothermic peak during the first heating cycle ranging from 198 to 232 °C and no peaks during the cooling cycle. The heat of fusion enthalpy ΔH_m for $Zn(L1)_2$ to $Zn(L4)_2$ was 33, 44, 20, and 32 J g^{-1}, respectively, and the fusion entropy ΔS_m follow the same trend: ΔS_m for $Zn(L1)_2$ to $Zn(L4)_2$ were 68, 88, 42, and 63 J K^{-1} kg^{-1}, respectively, as shown in Table 3. These results are consistent with $Zn(L1–L4)_2$, melting into an isotropic liquid upon heating, followed by glass formation upon cooling.[17] Conventional melting point measurements confirmed that the endothermic peak for $Zn(L1–L4)_2$ is a crystal-melting phase transition. The substitution of phenyl groups in $Zn(L1)_2$ with 1-naphthyl groups ($Zn(L2)_2$) increased the crystallinity because the melting temperature and ΔH_m increased by 19 °C and 11 J g^{-1}, respectively. On the other hand, substitution with 2-naphthyl lowered the crystallinity since the melting point and ΔH_m decreased by 12 °C and 13 J g^{-1} compared to $Zn(L1)_2$, respectively. Substitution with the larger 9-phenanthrenyl groups increased the melting point by 22 °C but did not affect ΔH_m or ΔS_m significantly compared to $Zn(L1)_2$.

Table 3. Thermal Properties of Zinc(II) Complexes

compound	fusion enthalpy ΔH_m (J g^{-1})	fusion entropy ΔS_m (J K^{-1} kg^{-1})	melting temperature (K)
$Zn(L1)_2$	33	68	483
$Zn(L2)_2$	44	88	502
$Zn(L3)_2$	20	42	471
$Zn(L4)_2$	32	63	505

Crystallography. All zinc(II) complexes were successfully crystallized by dissolving the complexes in a solvent mixture of dichloromethane and acetonitrile in a volume ratio of 8:1, followed by slow evaporation of dichloromethane from the mixture. All crystals were dark purple in appearance. Visually, the crystals of $Zn(L1)_2$ and $Zn(L2)_2$ were diamond-shaped and $Zn(L3)_2$ and $Zn(L4)_2$ were flake-shaped. Figure 5 shows the ellipsoid plot of $Zn(L1–L4)_2$. All zinc(II) complexes exhibit a distorted tetrahedral structure with intramolecular $\pi–\pi$ stacking in four places between a proximal phenyl of one ligand and a pyrrole ring of the other ligand. The dihedral angles between the two ligands and the intramolecular $\pi–\pi$ stacking distances are summarized in Table 4. The aryl group slightly influences the dihedral angle, ranging from 72.2° for $Zn(L2)_2$ to 67.5° for $Zn(L4)_2$, as well as the intramolecular $\pi–\pi$ stacking distance, ranging from 3.57 Å for $Zn(L4)_2$ to 3.82 Å for $Zn(L1)_2$.

In contrast, the pyrrolic aryl group strongly affects the molecular packing in crystals. In the context of understanding charge transport, we analyzed possible $\pi–\pi$ interactions between adjacent molecules in the crystal. Unlike with the fluorinated complex, we found neither sandwich (S, also called co-facial) nor parallel-displaced (P) $\pi–\pi$ interactions between the aryls of the pyrrolic groups (denoted pyrrolic) of adjacent molecules. Instead, we found T-shaped (T, also called face-to-edge)-type intermolecular interactions between the pyrrolic of one molecule and other parts of another molecule, as depicted in Figure 5 and summarized in Table 4. This is not too surprising since unsubstituted acenes tend to crystallize in herringbone patterns in which the molecules interact face-to-edge (T-shaped) through C–H···π interactions.[18] The distances between the centroids of aromatic rings observed for our molecules were in the range of 4.0–4.8 Å, and the dihedral angles between aromatic rings in the T-shaped $\pi–\pi$ interactions varied from 23 to 57° (see Table 4 and Figure S13). The distances do not appear to correlate with the size of the aryl groups. This observation is consistent with the aryl groups having weak interactions that are not strong enough to facilitate structural assembly.[19] For comparison, the distance and angle for pentacene are 4.7 Å and 53°, respectively, using our measurement method applied to the published pentacene crystal structure, see Figure S13.[20] We conclude that the distances we observed for the T-shaped intermolecular interactions are within the range possible for good charge transport.

https://dx.doi.org/10.1021/acs.jpcc.0c00401
J. Phys. Chem. C 2020, 124, 8541−8549

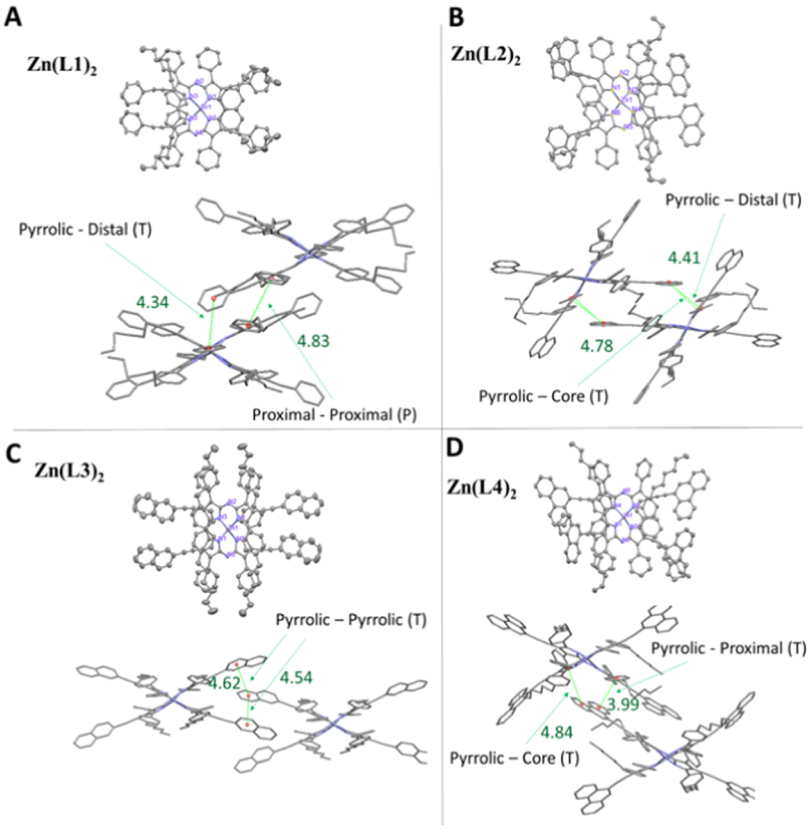

Figure 5. Ellipsoid plots of (A) $Zn(L1)_2$, (B) $Zn(L2)_2$, (C) $Zn(L3)_2$, and (D) $Zn(L4)_2$. The hydrogen atoms and dichloromethane solvate were omitted for clarity. Intermolecular $\pi-\pi$ stacking was shown in the stick model for each zinc complex. Data and figures are extracted from single-crystal X-ray diffraction (XRD) files by using Mercury 3.10.2. The distances were measured between the centroids of aromatic rings.

Table 4. Summary of $\pi-\pi$ Stacking Types, Distances, and Dihedral Angles from the Crystallographic Data of Zinc(II) Complexes[a]

compound	intramol. dihedral angle (deg)	intramol. distance (Å)[b]	intermol. type[c]	intermol. distance (Å)[c] and dihedral angle (deg)[d]
$Zn(L1)_2$	70.7	3.82	pyrrolic–distal (T), proximal–proximal (P)	4.34 (40°), 4.83
$Zn(L2)_2$	72.2	3.73	pyrrolic–core (T), pyrrolic–distal (T)	4.78 (53°), 4.42 (23°)
$Zn(L3)_2$	71.3	3.62	pyrrolic–pyrrolic (T), pyrrolic–pyrrolic (T)	4.54 (57°), 4.62 (57°)
$Zn(L4)_2$	67.5	3.57	pyrrolic–proximal (T), pyrrolic–core (T)	3.99 (35°), 4.84 (63°)

[a]Distal, proximal, pyrrolic, and core refer to the distal phenyl ring, proximal phenyl ring, pyrrolic aryl ring, and pyrrole ring, respectively. Intermolecular $\pi-\pi$ stacking types are sandwich (S), T-shaped (T), and parallel-displaced (P) $\pi-\pi$ stacking. [b]Intramolecular $\pi-\pi$ stacking distance. [c]Intermolecular $\pi-\pi$ stacking type or distance. [d]Dihedral angle for the corresponding T-shaped $\pi-\pi$ stacking.

Photovoltaic Properties. Photovoltaic properties were investigated using an inverted configuration: ITO/ZnO/P3HT:n-type/MoO_3/Ag. Device processing optimization involved screening for the P3HT:zinc(II) complex blend weight ratios, total concentration, and annealing conditions; optimization details are summarized in Tables S1–S7. Figure 6A shows the current density–voltage curves of the best devices, and the performance parameters are summarized in Table 4. The best PCE obtained was 3.0, 5.5, 3.7, and 3.4% for $Zn(L1)_2$, $Zn(L2)_2$, $Zn(L3)_2$, and $Zn(L4)_2$, respectively. The 5.5% PCE for the $Zn(L2)_2$ cell is among the best-reported performances for P3HT-based OPV, due to the high V_{OC}, J_{SC},

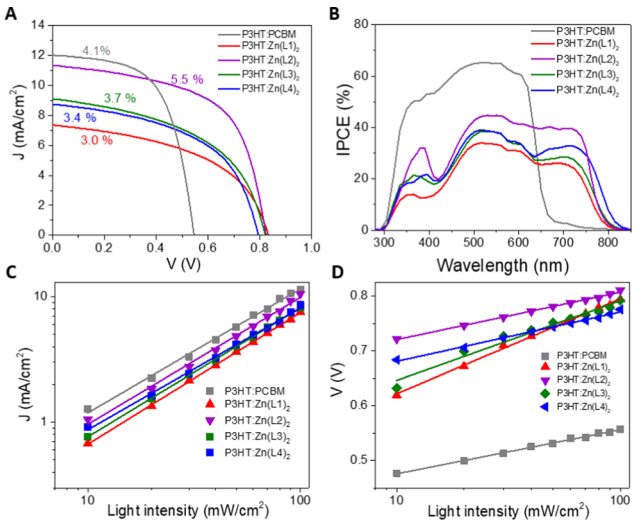

Figure 6. (A) Current density–voltage characteristics of solar cells with an effective area of 0.2 cm^2 using simulated AM1.5G illumination at 100 mW cm^{-2}; (B) incident photon-to-current efficiency (IPCE) spectra of solar cells. (C) J_{SC} as a function of light intensity on a double-logarithmic scale and (D) V_{OC} as a function of light intensity on a semilogarithmic scale. The fill factor for all cells did not change much with light intensity ranging from 10 to 100 mW cm^{-2}.

https://dx.doi.org/10.1021/acs.jpcc.0c00401
J. Phys. Chem. C 2020, 124, 8541–8549

Table 5. Performance Parameters, Power-Law Exponents, and V_{OC} Slopes of OPVs[a]

n-type material	V_{OC} (V)	J_{SC} (mA cm^{-2})	FF (%)	PCE (%)	power-law exponent	V_{OC} slope (times of kT/q)
Zn(L1)$_2$	0.81 (0.80 ± 0.03)	7.5 (7.3 ± 0.3)	49 (49 ± 2)	3.0 (2.8 ± 0.2)	1.05	2.0
Zn(L2)$_2$	0.82 (0.82 ± 0.01)	11.3 (10.8 ± 0.7)	59 (59 ± 3)	5.5 (5.2 ± 0.3)	1.01	1.3
Zn(L3)$_2$	0.82 (0.81 ± 0.02)	9.1 (8.5 ± 0.6)	50 (49 ± 2)	3.7 (3.3 ± 0.4)	1.03	2.4
Zn(L4)$_2$	0.76 (0.76 ± 0.03)	8.8 (8.6 ± 0.3)	50 (50 ± 2)	3.5 (3.3 ± 0.2)	0.97	1.6
PCBM	0.54 (0.54 ± 0.02)	12.0 (11.5 ± 0.6)	63 (63 ± 1)	4.1 (4.0 ± 0.2)	0.99	1.2

[a]For solar cells, all n-type materials were tested by blending with P3HT using optimized conditions. Averages were calculated for at least six devices. k is Boltzmann's constant, T is the temperature, and q is the elementary charge.

Table 6. Charge Carrier Mobility and Calculated Charge-Transfer Integral V of Zinc(II) Complexes[a]

compound	neat μ_h (cm^2 V^{-1} s^{-1})	neat μ_e (cm^2 V^{-1} s^{-1})	blend μ_h (cm^2 V^{-1} s^{-1})	blend μ_e (cm^2 V^{-1} s^{-1})	V hole (meV)	V electron (meV)
Zn(L1)$_2$	9.0×10^{-7}	3.2×10^{-5}	3.0×10^{-4}	4.0×10^{-5}	2.4	−0.5
Zn(L2)$_2$	1.0×10^{-4}	4.2×10^{-5}	3.1×10^{-4}	2.4×10^{-5}	−3.5	−3.4
Zn(L3)$_2$	1.5×10^{-6}	3.1×10^{-5}	2.0×10^{-4}	8.4×10^{-6}	−2.4	−0.6
Zn(L4)$_2$	1.1×10^{-6}	2.7×10^{-5}	3.1×10^{-4}	1.3×10^{-5}	−3.9	−1.9
PCBM		5.0×10^{-5}[b]	5.5×10^{-4}[b]	2.6×10^{-3}[b]		

[a]A minimum of four devices were made for each mobility measurement and the average values are reported. Blend mobilities were measured from blends of n-type materials and P3HT using the same fabrication method as for optimized solar cells. [b]Published data.[15]

and FF being 0.83 V, 11.3 mA cm^{-2}, and 59%, respectively.[21−23]

To better understand the PCE differences, we analyzed the device performance parameters. All zinc(II) complex cells have higher open-circuit voltages (V_{OC}, ∼ 0.8 V) than the reference PCBM cell (0.54 V) due to the higher LUMO energy level of the zinc(II) complexes. Replacing the pyrrolic phenyls with larger aryl groups increases the J_{SC} from 7.5 mA cm^{-2} for Zn(L1)$_2$ to 11.3, 9.1, and 8.8 mA cm^{-2} for Zn(L2)$_2$, Zn(L3)$_2$ and Zn(L4)$_2$, respectively. The FF is ∼50% for most complexes, except for Zn(L2)$_2$, which is higher (at 59%), consistent with its higher J_{SC}. Figure S14 shows the UV−vis absorption of P3HT:zinc(II) complex blend films made under the same optimized conditions for active layer fabrication in the solar cell. A rough integration of the light absorption (denoted by a.u.) from 300 to 850 nm indicates that P3HT:Zn(L2−L4)$_2$ films have similar absorption, around 102 and −118 a.u., which is not sufficient to explain the over 20% J_{SC} drop from P3HT:Zn(L2)$_2$ OPVs to P3HT:Zn(L3−L4)$_2$ OPVs. The J_{SC} decreases are consistent with decreases in the incident photon-to-current efficiencies (IPCEs, Figure 5B): IPCE at 510 nm was 34, 44, 39, and 39% for Zn(L1−L4)$_2$, respectively. The maximum IPCEs of the zinc(II) complex cells are generally lower than those of PCBM cells because the optimized cell thickness of the zinc(II) complex cells is smaller, ∼80 nm, than that of the PCBM cell, ∼190 nm, thus limiting the absorption for the zinc(II) complex cells. The J_{SC} and IPCE trends observed within the zinc(II) complex series cannot be explained from absorption differences alone and must depend on other factors affecting photocurrent, such as free charge generation, electron−hole pair separation, and charge carrier recombination.

To further understand the OPV results, charge recombination was investigated from J−V light intensity dependence measurements. Figure 6C shows the J_{SC} as a function of light intensity on a double-logarithmic scale, and the extracted power-law exponents for all solar cells are reported in Table 5. All power-law exponents were close to unity, indicating that the loss from bimolecular recombination in all optimized cells is small.[24]Figure 6D shows the V_{OC} as a function of light intensity on a semilogarithmic scale. There is a monotonic relationship between V_{OC} and the light intensity. The data were fitted into a linear function, and the extracted slopes, presented as multiples of kT/q, are summarized in Table 5. A slope of $1kT/q$ indicates that only Langevin recombination is present, and a higher slope means that trap-assisted recombination is also present.[24,25] The slope for P3HT:PCBM cells, $1.2kT/q$, is close to the reported data, $1.4kT/q$, for P3HT:PCBM cells under similar fabrication conditions.[26] Since PCBM is a trap-free material, the carrier traps in the P3HT:CBM cell are assumed to be mainly induced by P3HT.[27] The slopes for Zn(L1)$_2$, Zn(L2)$_2$, Zn(L3)$_2$, and Zn(L4)$_2$ cells are 2.0, 1.3, 2.4, and 1.6 times kT/q, respectively, indicating Zn(L3)$_2$ has the largest loss from trap-assisted recombination, followed by Zn(L1)$_2$ and Zn(L4)$_2$. Zn(L2)$_2$ has the lowest trap-assisted recombination. This is consistent with the J_{SC} and PCE trends in OPVs and partially explains the high J_{SC} and high FF in Zn(L2)$_2$ cells. Nevertheless, Zn(L3)$_2$ does not fit this trend as Zn(L3)$_2$ cells have the largest trap-assisted recombination, yet has a higher J_{SC} and PCE compared to Zn(L1)$_2$ and Zn(L4)$_2$. Thus, other factors must also play important roles in these systems.

Charge-Transport Properties. The space-charge-limited current (SCLC) method was used to measure the charge carrier mobility of zinc(II) complexes in neat and blend films. Hole mobility (μ_h) measurement was done using a device structure of ITO/PEDOT:PSS/active layer/MoO_3/Ag, and electron mobility (μ_e) measurement was done using a device structure of ITO/ZnO/active layer/Ca/Al. The charge mobility was calculated with the Mott−Gurney law under the trap-free SCLC situation using the equation

$$J = \frac{9\varepsilon_r\varepsilon_0\mu V^2}{8L^3} \quad (1)$$

where J is the current, ε_0 is the permittivity of free space, ε_r is the relative permittivity of the material, μ is the charge carrier mobility, V is the effective voltage, and L is the thickness of the active layer.[28] The SCLC graphs are shown in Figure S15, and the results are summarized in Table 6. The film electron mobility of all neat zinc(II) complexes varied slightly within the same magnitude, ranging from 2.7×10^{-5} to 4.2×10^{-5} cm^2 V^{-1} s^{-1}. Interestingly, all zinc(II) complexes have similar

https://dx.doi.org/10.1021/acs.jpcc.0c00401
J. Phys. Chem. C 2020, 124, 8541−8549

hole mobility, around 1×10^{-6} cm^2 V^{-1} s^{-1}, except for Zn(L2)$_2$, which exhibits a hole mobility of 1.1×10^{-4} cm^2 V^{-1} s^{-1}. This is about 2 orders of magnitude higher than that for other zinc(II) complexes and is close to the reported hole mobility of the pristine P3HT film, $(1.4-3) \times 10^{-4}$ cm^2 V^{-1} s^{-1}.[29] This indicates that Zn(L2)$_2$ can not only transport electrons, but the intermolecular interaction in Zn(L2)$_2$ also facilitates hole transport in neat films. The low electron mobilities explain why our optimized OPVs are limited to film thicknesses of 80 nm.

To better understand charge transport in these systems, we turned to theoretical calculations. According to the Marcus theory, there are two major parameters that determine intermolecular charge transfer and thus charge carrier mobility in molecular systems: reorganization energy, which must be minimized, and electronic coupling, which must be maximized.[18,30] We have shown that these types of complexes tend to have very low reorganization energies due to their large and rigid π-conjugated system that extends across the two azadipyrromethene ligands via interligand $\pi-\pi$ interactions.[31] As discussed in the Crystallography Section, the main type of intermolecular $\pi-\pi$ stacking observed in crystals was T-shaped, with distances in the range for good charge transport. While T-shaped type interactions are not as good as S- and P-type interactions for charge transport, they can lead to high charge carrier mobility in some cases, provided the orbital overlap is large.[18,32] An example of a high-mobility material (up to 2.0 cm^2 V^{-1} s^{-1})[33] with herringbone packing is pentacene, where the $\pi-\pi$ interactions are T-shaped.[20] To estimate the overlap integrals of our complexes, we performed single-point energy calculations of the molecular dimers. The molecular dimers were obtained from the crystal structure (Figure 5), and the charge-transfer integral V was calculated using density functional theory (DFT) in the Amsterdam density functional (ADF) code.[34−38] Table 6 summarizes the results. Since charge transport is proportional to V^2, the sign of V does not matter. According to the calculations, $|V|$ is in the 2.4−3.9 meV range for hole transport and 0.5−1.9 meV range for electron transport. These values are relatively small compared to the value calculated under the same conditions for pentacene, at 64 and −50 meV for hole and electron transfer, respectively. This calculation, therefore, suggests that charge transport will be roughly 10^2 to 10^3 times smaller than that of pentacene for hole transport and 10^2 to 10^4 times lower than that of pentacene for electron transport. The overlap integrals are therefore consistent with the low mobilities observed. However, it is hard to directly correlate the trend of overlap integrals with the trend of mobility of zinc complexes in the film because this calculation is based on the condition of the single crystal rather than the films, which have a disordered crystal structure and different crystalline density.[38]

The blend film mobilities of zinc(II) complexes were also studied. After blending with P3HT, Zn(L1)$_2$, Zn(L2)$_2$, and Zn(L4)$_2$ showed similar electron mobility to that in neat films, in the magnitude of 10^{-5} cm^2 V^{-1} s^{-1}. However, the mobility of Zn(L3)$_2$ dropped from 3.1×10^{-5} cm^2 V^{-1} s^{-1} in the neat film to 8.4×10^{-6} cm^2 V^{-1} s^{-1} in the blend film. This suggests that the 2-naphthyl groups on the pyrrolic position may negatively affect the phase separation between the zinc complex and P3HT in blends. The hole mobility for all P3HT:zinc(II) complex blends was $\sim 2 \times 10^{-4}$ cm^2 V^{-1} s^{-1}, which is attributed to the hole transport in P3HT. This suggests that the zinc complexes do not interfere with P3HT self-assembly in films.

Morphology. The surface morphology of the optimized cell films was studied by tapping-mode atomic force microscopy (AFM). The phase and height images for all zinc(II) complex cells are shown in Figure 7. The height images show that the films are smooth, with surface roughness ranging from 12 to 5 nm. The phase images show more defined features, with lighter and darker parts related to domains having different adhesion and mechanical properties.[39] The two materials appear to be phase-separated with irregular-shaped domains of 25−50 nm for P3HT:Zn(L1)$_2$, 15−40 nm for the P3HT:Zn(L2)$_2$ blends, and 10−50 nm for P3HT:Zn(L3)$_2$ and P3HT:Zn(L4)$_2$ blends. The smaller domain size ranges observed for the P3HT:Zn(L2)$_2$ blends are expected to be more favorable for electron−hole pair splitting and charge generation than the domain size range of the other three blends.

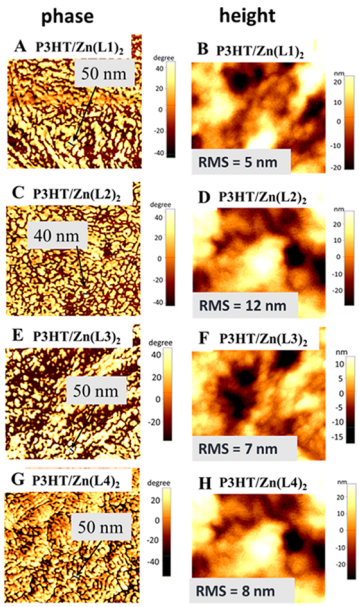

Figure 7. (A), (C), (E), and (G) show phase images for the optimized OPV films of P3HT:Zn(L1)$_2$, P3HT:Zn(L2)$_2$, P3HT:Zn(L3)$_2$, and P3HT:Zn(L4)$_2$, respectively. (B), (D), (F), and (H) show height images for P3HT:Zn(L1)$_2$, P3HT:Zn(L2)$_2$, P3HT:Zn(L3)$_2$, and P3HT:Zn(L4)$_2$, respectively. In phase images, dark and bright parts can be differentiated as different components. All films were annealed at the same conditions as optimized OPVs and all images are 1 μm × 1 μm.

■ CONCLUSIONS

Two zinc(II) ADP complexes, Zn(L3)$_2$ and Zn(L4)$_2$, have been successfully synthesized through pyrrolic substitution, and all starting materials used for the synthesis are cheap and easy to obtain. Four zinc(II) complexes, Zn(L1−L4)$_2$, were compared in a series to investigate the structure−property relationship. The substitution of phenyl with larger aryl groups slightly improved the absorptivity and red-shifted the absorbance. The substitutions have almost no effect on the HOMO and LUMO energy levels. Crystals of Zn(L1−L4)$_2$ were obtained, and different aryl groups on the pyrrolic positions led to different packing modes in solid states. All complexes showed T-shaped intermolecular interactions

https://dx.doi.org/10.1021/acs.jpcc.0c00401
J. Phys. Chem. C 2020, 124, 8541−8549

involving the aryl group in the pyrrolic position. Using 1-naphthyl gave the highest crystallinity compared to 2-naphthyl and 9-phenanthrenyl. The OPV performances of $Zn(L3)_2$ (PCE of 3.7%) and $Zn(L4)_2$ (PCE of 3.4%) were lower than that of $Zn(L2)_2$, PCE of 5.5%, due to the higher trap-assisted recombination and less favorable morphology. The mobility in these complexes tends to be low, limiting their performance in OPVs. Calculations suggest that the low mobilities are due to the relatively low overlap integrals. The size and anchoring position of the aryl group have a large effect on the properties, and increasing the aryl size from naphthyl to phenanthrenyl does not appear to enhance the intermolecular interactions and charge transport. We are currently looking into substituted aryl groups that could favor potentially stronger S- or P-type intermolecular $\pi-\pi$ interactions.

■ ASSOCIATED CONTENT

Supporting Information

The Supporting Information is available free of charge at https://pubs.acs.org/doi/10.1021/acs.jpcc.0c00401.

Experimental section; NMR spectra; MALDI-TOF MS spectra; UV−vis spectra and TGA; Ellipsoid plots of $Zn(L1-L4)_2$; illustration of intermolecular $\pi-\pi$ interactions; OPV optimization details; mobility measurements; AFM images; crystal data for the zinc complexes (PDF)

$Zn(L3)_2$ (CCDC = 1971189) (CIF)

$Zn(L4)_2$ (CCDC = 1971190) (CIF)

■ AUTHOR INFORMATION

Corresponding Author

Geneviève Sauvé − *Department of Chemistry, Case Western Reserve University, Cleveland, Ohio 44106, United States;* orcid.org/0000-0002-9721-0447; Email: genevieve.sauve@case.edu

Authors

Chunlai Wang − *Department of Chemistry, Case Western Reserve University, Cleveland, Ohio 44106, United States*

Muyuan Zhao − *Department of Chemistry, Case Western Reserve University, Cleveland, Ohio 44106, United States*

Arnold L. Rheingold − *Department of Chemistry and Biochemistry, University of California, San Diego, San Diego, California 92093, United States;* orcid.org/0000-0003-4472-8127

Complete contact information is available at: https://pubs.acs.org/10.1021/acs.jpcc.0c00401

Author Contributions

The manuscript was written through the contributions of all authors. All authors have given approval to the final version of the manuscript.

Notes

The authors declare no competing financial interest.

■ ACKNOWLEDGMENTS

We are grateful to the National Science Foundation (CHEM 1904868 and CHEM 1148652) for funding this project. We thank Dr. Peiran Wei for collecting the AFM images, Dr. John D. Protasiewicz for access to cyclic voltammetry instrumentation, and the Materials for Optoelectronics Research and Education (MORE) Center at CWRU for device fabrication and characterization. We thank Prof. Advincula at CWRU for access to his AFM instruments. This project was possible, thanks to NSF MRI-0821515 for MALDI-TOF-TOF instrumentation and NSF MRI-1334048 for NMR instrumentation.

■ REFERENCES

(1) Loudet, A.; Burgess, K. BODIPY Dyes and Their Derivatives: Syntheses and Spectroscopic Properties. *Chem. Rev.* **2007**, *107*, 4891−4932.

(2) Partyka, D.; Deligonul, N.; Washington, M.; Gray, T. Fac-Tricarbonyl Rhenium(I) Azadipyrromethene Complexes. *Organometallics* **2009**, *28*, 5837−5840.

(3) Palma, A.; Gallagher, J. F.; Mueller-Bunz, H.; Wolowska, J.; McInnes, E. J. L.; O'Shea, D. F. Co(II), Ni(II), Cu(II) and Zn(II) Complexes of Tetraphenylazadipyrromethene. *Dalton Trans.* **2009**, 273−279.

(4) Ge, Y.; O'Shea, D. F. Azadipyrromethenes: From Traditional Dye Chemistry to Leading Edge Applications. *Chem. Soc. Rev.* **2016**, *45*, 3846−3864.

(5) Mueller, T.; Gresser, R.; Leo, K.; Riede, M. Organic Solar Cells Based on a Novel Infrared Absorbing Aza-BODIPY Dye. *Sol. Energy Mater. Sol. Cells* **2012**, *99*, 176−181.

(6) Leblebici, S. Y.; Catane, L.; Barclay, D. E.; Olson, T.; Chen, T. L.; Ma, B. Near-Infrared Azadipyrromethenes as Electron Donor for Efficient Planar Heterojunction Organic Solar Cells. *ACS Appl. Mater. Interfaces* **2011**, *3*, 4469−4474.

(7) Zhang, X.; Zhang, Y.; Chen, L.; Xiao, Y. Star-Shaped Carbazole-Based Bodipy Derivatives with Improved Hole Transportation and Near-Infrared Absorption for Small-Molecule Organic Solar Cells with High Open-Circuit Voltages. *RSC Adv.* **2015**, *5*, 32283−32289.

(8) Lorenz-Rothe, M.; Schellhammer, K. S.; Jaegeler-Hoheisel, T.; Meerheim, R.; Kraner, S.; Hein, M. P.; Schuenemann, C.; Tietze, M. L.; Hummert, M.; Ortmann, F.; Cuniberti, G.; Koerner, C.; Leo, K. From Fluorine to Fluorene-a Route to Thermally Stable Aza-BODIPYS for Organic Solar Cell Application. *Adv. Electron. Mater.* **2016**, *2*, No. 1600152.

(9) Mao, Z.; Senevirathna, W.; Liao, J. Y.; Gu, J.; Kesava, S. V.; Guo, C.; Gomez, E. D.; Sauvé, G. Azadipyrromethene-Based Zn(II) Complexes as Nonplanar Conjugated Electron Acceptors for Organic Photovoltaics. *Adv. Mater.* **2014**, *26*, 6290−6294.

(10) Wang, C.; Wei, P.; Ngai, J. H. L.; Rheingold, A. L.; Gray, T. G.; Li, Y.; Pentzer, E.; Li, R.; Zhu, L.; Sauvé, G. A Zinc(II) Complex of Di(Naphthylethynyl)Azadipyrromethene with Low Synthetic Complexity Leads to OPV with High Industrial Accessibility. *J. Mater. Chem. A* **2019**, *7*, 24614−24625.

(11) Senevirathna, W.; Liao, J.-y.; Mao, Z.; Gu, J.; Porter, M.; Wang, C.; Fernando, R.; Sauvé, G. Synthesis, Characterization and Photovoltaic Properties of Azadipyrromethene-Based Acceptors: Effect of Pyrrolic Substituents. *J. Mater. Chem. A* **2015**, *3*, 4203−4214.

(12) Po, R.; Bernardi, A.; Calabrese, A.; Carbonera, C.; Corso, G.; Pellegrino, A. From Lab to Fab: How Must the Polymer Solar Cell Materials Design Change? − an Industrial Perspective. *Energy Environ. Sci.* **2014**, *7*, 925−943.

(13) Sauvé, G.; Fernando, R. Beyond Fullerenes: Designing Alternative Molecular Electron Acceptors for Solution-Processable Bulk Heterojunction Organic Photovoltaics. *J. Phys. Chem. Lett.* **2015**, *6*, 3770−3780.

(14) Fernando, R.; Pejić, S.; Thomsen, A.; Wang, C.; Sauvé, G. Azadipyrromethene-Based near-Ir Dyes with Styryl Substituents at the Pyrrolic Positions for Organic Photovoltaic Applications. *Dyes Pigm.* **2019**, *168*, 257−263.

(15) Pejić, S.; Thomsen, A. M.; Etheridge, F. S.; Fernando, R.; Wang, C.; Sauvé, G. Fluorination Increases the Electron Mobility of Zinc Azadipyrromethene-Based Electron Acceptors and Enhances the Performance of Fullerene-Free Organic Solar Cells. *J. Mater. Chem. C* **2018**, *6*, 3990−3998.

(16) Etheridge, F. S.; Fernando, R. J.; Pejić, S.; Zeller, M.; Sauvé, G. Synthesis and Characterization of Fluorinated Azadipyrromethene

Complexes as Acceptors for Organic Photovoltaics. *Beilstein J. Org. Chem.* **2016**, *12*, 1925−1938.
(17) Ozdemir, M.; Choi, D.; Zorlu, Y.; Cosut, B.; Kim, H.; Kim, C.; Usta, H. A New Rod-Shaped Bodipy-Acetylene Molecule for Solution-Processed Semiconducting Microribbons in N-Channel Organic Field-Effect Transistors. *New J. Chem.* **2017**, *41*, 6232−6240.
(18) Mas-Torrent, M.; Rovira, C. Role of Molecular Order and Solid-State Structure in Organic Field-Effect Transistors. *Chem. Rev.* **2011**, *111*, 4833−4856.
(19) Zatsikha, Y. V.; et al. 1,7-Dipyrene-Containing Aza-BODIPYS: Are Pyrene Groups Effective as Ligands to Promote and Direct Complex Formation with Common Nanocarbon Materials? *J. Phys. Chem. C* **2018**, *122*, 27893−27916.
(20) Mattheus, C. C.; Dros, A. B.; Baas, J.; Meetsma, A.; de Boer, J. L.; Palstra, T. T. M. Polymorphism in Pentacene. *Acta Crystallogr., Sect. C: Cryst. Struct. Commun.* **2001**, *57*, 939−941.
(21) Baran, D.; et al. Reducing the Efficiency-Stability-Cost Gap of Organic Photovoltaics with Highly Efficient and Stable Small Molecule Acceptor Ternary Solar Cells. *Nat. Mater.* **2017**, *16*, 363−369.
(22) Holliday, S.; et al. High-Efficiency and Air-Stable P3HT-Based Polymer Solar Cells with a New Non-Fullerene Acceptor. *Nat. Commun.* **2016**, *7*, No. 11585.
(23) Xiao, B.; Tang, A.; Zhang, J.; Mahmood, A.; Wei, Z.; Zhou, E. Achievement of High Voc of 1.02 V for P3HT-Based Organic Solar Cell Using a Benzotriazole-Containing Non-Fullerene Acceptor. *Adv. Energy Mater.* **2017**, *7*, No. 1602269.
(24) Proctor, C. M.; Kuik, M.; Nguyen, T.-Q. Charge Carrier Recombination in Organic Solar Cells. *Prog. Polym. Sci.* **2013**, *38*, 1941−1960.
(25) Mandoc, M. M.; Veurman, W.; Koster, L. J. A.; de Boer, B.; Blom, P. W. M. Origin of the Reduced Fill Factor and Photocurrent in MDMO-PPV: PCNEPV All-Polymer Solar Cells. *Adv. Funct. Mater.* **2007**, *17*, 2167−2173.
(26) Nalwa, K. S.; Kodali, H. K.; Ganapathysubramanian, B.; Chaudhary, S. Dependence of Recombination Mechanisms and Strength on Processing Conditions in Polymer Solar Cells. *Appl. Phys. Lett.* **2011**, *99*, No. 263301.
(27) Brabec, C.; Cravino, A.; Meissner, D.; Sariciftci, N. S.; Fromherz, T.; Sanchez, L.; Hummelen, J. C. Origin of the Open Circuit Voltage of Plastic Solar Cells. *Adv. Funct. Mater.* **2001**, *11*, 374−380.
(28) Unlu, N. A.; Hacioglu, S. O.; Hizalan, G.; Yildiz, D. E.; Toppare, L.; Cirpan, A. Benzodithiophene and Benzotriazole Bearing Conjugated Polymers for Electrochromic and Organic Solar Cell Applications. *J. Electrochem. Soc.* **2017**, *164*, G71−G76.
(29) Laquai, F.; Andrienko, D.; Mauer, R.; Blom, P. W. Charge Carrier Transport and Photogeneration in P3HT:PCBM Photovoltaic Blends. *Macromol. Rapid Commun.* **2015**, *36*, 1001−1025.
(30) Marcus, R. A. Electron Transfer Reactions in Chemistry: Theory and Experiment (Nobel Lecture). *Angew. Chem., Int. Ed.* **1993**, *32*, 1111−1222.
(31) Senevirathna, W.; Daddario, C. M.; Sauvé, G. Density Functional Theory Study Predicts Low Reorganization Energies for Azadipyrromethene-Based Metal Complexes. *J. Phys. Chem. Lett.* **2014**, *5*, 935−941.
(32) Anthony, J. E. The Larger Acenes: Versatile Organic Semiconductors. *Angew. Chem., Int. Ed.* **2008**, *47*, 452−483.
(33) Biring, S.; Li, Y.-Z.; Lee, C.-C.; Pan, A.; Li, Y.-D.; Kumar, G.; Liu, S.-W. The Effect of Gate Dielectric Deposition at Different Vacuum Conditions on the Field-Effect Mobility of Pentacene Based Organic Field Effect Transistors. *Thin Solid Films* **2017**, *636*, 485−489.
(34) te Velde, G.; Bickelhaupt, F. M.; Baerends, E. J.; Foseca Guerra, C.; Van Gisbergen, S. J. A.; Snijders, J. G.; Ziegler, T. Chemistry with ADF. *J. Comput. Chem.* **2001**, *22*, 931−967.
(35) ADF 2019.3, SCM, *Theoretical Chemistry*; Vrije Universiteit: Amsterdam, the Netherlands, http://www.Scm.Com.
(36) Seldenthuis, J. S. Electrical and Mechanical Effects in Single-Molecule Junctions. Ph.D. Thesis; Delft University of Technology, 2011.
(37) Verzijl, C. J. O.; Seldenthuis, J. S.; Thijssen, J. M. Applicability of the Wide-Band Limit in Dft-Based Molecular Transport Calculations. *J. Chem. Phys.* **2013**, *138*, No. 094102.
(38) Deng, W.-Q.; Sun, L.; Huang, J.-D.; Chai, S.; Wen, S.-H.; Han, K.-L. Quantitative Prediction of Charge Mobilities of π-Stacked Systems by First-Principles Simulation. *Nat. Protoc.* **2015**, *10*, 632−642.
(39) Liu, Y.; Chen, C. C.; Hong, Z.; Gao, J.; Yang, Y. M.; Zhou, H.; Dou, L.; Li, G.; Yang, Y. Solution-Processed Small-Molecule Solar Cells: Breaking the 10% Power Conversion Efficiency. *Sci. Rep.* **2013**, *3*, No. 3356.

https://dx.doi.org/10.1021/acs.jpcc.0c00401
J. Phys. Chem. C 2020, 124, 8541−8549